4 | Galaxy alignments in massive clusters from ~14,000 spectroscopic members

Torques acting on galaxies lead to physical alignments, but the resulting ellipticity correlations are difficult to predict. As they constitute a major contaminant for cosmic shear studies, it is important to constrain the intrinsic alignment signal observationally. We measured the alignments of satellite galaxies within 90 massive galaxy clusters in the redshift range $0.05 < z < 0.55$ and quantified their impact on the cosmic shear signal. We combined a sample of 38,104 galaxies with spectroscopic redshifts with high-quality data from the Canada-France-Hawaii Telescope. We used phase-space information to select 14,576 cluster members, 14,250 of which have shape measurements and measured three different types of alignment: the radial alignment of satellite galaxies toward the brightest cluster galaxies (BCGs), the common orientations of satellite galaxies and BCGs, and the radial alignments of satellites with each other. Residual systematic effects are much smaller than the statistical uncertainties. We detect no galaxy alignment of any kind out to at least $3r_{200}$. The signal is consistent with zero for both blue and red galaxies, bright and faint ones, and also for subsamples of clusters based on redshift, dynamical mass, and dynamical state. These conclusions are unchanged if we expand the sample with bright cluster members from the red sequence. We augment our constraints with those from the literature to estimate the importance of the intrinsic alignments of satellites compared to those of central galaxies, for which the alignments are described by the linear alignment model. Comparison of the alignment signals to the expected uncertainties of current surveys such as the Kilo-Degree Survey suggests that the linear alignment model is an adequate treatment of intrinsic alignments, but it is not clear whether this will be the case for larger surveys.

4.1.   Introduction

Tidal torques tend to align triaxial satellite galaxies toward the centre of the larger "host" gravitational potential as they orbit around its centre. This mechanism is well established in numerical simulations, where galaxies are typically locked pointing toward the centres of clusters, possibly with brief periodic misalignments depending on the specific orbit, well within a Hubble time (e.g., **?????**). In a hierarchical clustering scenario, this effect could be coupled with alignments arising from the nonlinear evolution of structure. Therefore the patterns and evolution of galaxy alignments—if any—contain important information about the initial conditions that gave rise to the present-day cosmic web, as well as the formation history and environments of galaxies.

Additionally, these galaxy alignments (commonly referred to as "intrinsic," as opposed to apparent, alignments) are a potential contaminant of cosmic shear, which is a measurment of the coherent distortions of galaxies in the background of a matter distribution. While the signal from these intrinsic alignments is weak enough that it is not relevant for weak lensing measurements of galaxy clusters (and in general cluster members can be identified and removed to a sufficient level), it is a concern for large-area cosmic shear surveys, which are more susceptible to this contamination, and where the requirements on precision and accuracy are more stringent. The contamination induced by these galaxy alignments into cosmic shear measurements can be divided into two effects. The first effect is the tidal alignment of galaxies with similar formation histories, so-called intrinsic-intrinsic or II signal. Since this effect is restricted to pairs with common formation or evolutionary histories, this II signal can be avoided by selecting pairs of galaxies with large angular and/or redshift separations (e.g., **???**). The second effect is more subtle and more difficult to control: the same gravitational field that aligns galaxies within a halo is responsible for the deflection of the light coming from background galaxies (**?**). This effect is referred to as gravitational-intrinsic or GI signal (for consistency, the lensing signal itself is referred to as gravitational-gravitational, or GG, signal). In tomographic analyses, it is possible to account for this effect through its distinct redshift dependence (**????**) or, inversely, to measure it from cosmic shear data by boosting its signal while suppressing the contribution from gravitational lensing (**?**). This cross-correlation has recently been shown to exist also between galaxy-galaxy lensing and CMB lensing (**??**). Intrinsic alignments can also be modeled directly in cosmic shear data and marginalized over to extract cosmological parameters (**??**). In an attempt to identify a consistent model for galaxy shapes and alignments, **??** have tried to match semi-analytical models to galaxies from the COSMOS survey (**?**) and find that the intrinsic alignment contamination to upcoming cosmic shear surveys should be $< 10\%$.

Recent large photometric and spectroscopic surveys such as the 2-degree Field redshift survey (2dF, **?**) and the Sloan Digital Sky Survey (SDSS, **?**) have allowed the study of galaxy alignments out to several tens of Mpc exploiting cross-correlation techniques, with robust direct detections of the GI signal up to $z \sim 0.7$ between galaxy samples with large line-of-sight separations (**???**), although **?** reported a null detection. However, the II signal is much weaker than the GI signal in nontomographic studies at intermediate redshifts typical of these surveys, and has typically eluded detection (e.g., **???**).

On smaller scales the history of these measurements goes back further, but the issue is far from settled. Early measurements of galaxy alignments focused on galaxy clusters, trying to understand galaxy formation and (co-)evolution. **?** were the first to claim a detection of a preferential direction of galaxies in clusters. Specifically, they found that satellite galaxies in Abell 2199 tend to point in the direction of the major axis of the BCG. However, most

subsequent measurements have been consistent with random orientations of satellite galaxies in clusters (e.g., ???????), although some authors have also claimed significant nonrandom orientations of these cluster satellites (e.g., ?????).

More recent studies have focused on smaller mass galaxy groups, where the number of objects is much larger. Similar to the results summarized above, most of these measurements are consistent with no alignments (????), although there are claims of significant detections (e.g., ??).[1] Interestingly, although this effect might be expected to be stronger for more massive haloes, ? found that satellite galaxies are radially aligned in galaxy-scale haloes. However, ? and ? have shown that the results can depend on the method used to estimate the direction of the satellite galaxies, so each result must be taken with care.

In general, there is clear tension between observations and numerical N-body simulations, with the latter predicting much higher signals than have been observed. This discrepancy can be attributed, for instance, to a misalignment between stars and dark matter, such that stars—being more centrally concentrated than dark matter—react more slowly and less strongly to tidal torquing from the parent halo (??). Whatever the physical reasons of this discrepancy, the potential impact of the choice of intrinsic alignment *model* on cosmological parameter estimation (?) makes it imperative that we know the level of intrinsic alignments to high precision at all relevant mass and spatial scales, and this can only be achieved through detailed observations.

In this work, we study the alignments of galaxies in clusters from a sample of galaxy clusters with high-quality photometric observations and a large number of spectroscopic redshifts from archival sources. We measure different kinds of alignments, assess systematic errors, and use the halo model to characterize galaxy alignments in the context of upcoming cosmic shear analyses.

We adopt a flat ΛCDM cosmology with $\Omega_\Lambda = 0.7$, Ω_m and $H_0 = 70\,\mathrm{km\,s^{-1}\,Mpc^{-1}}$. To calculate the power spectra, we use $\sigma_8 = 0.8$, $\Omega_b h^2 = 0.0245$, and $n_s = 1.0$. All magnitudes are MAG_AUTO from SExtractor in the AB system, and all absolute magnitudes and luminosities are in the rest frame of the corresponding cluster.

4.2. Data

4.2.1. Cluster sample and photometry

The cluster sample is drawn from two large, nonoverlapping X-ray selected cluster surveys carried out with the Canada-France-Hawaii Telescope (CFHT), namely the Multi-Epoch Nearby Cluster Survey (MENeaCS; ?) and the Canadian Cluster Comparison Project (CCCP; ?). MENeaCS performed multi-epoch observations of 57 clusters in the redshift range $0.05 < z < 0.15$, aimed at measuring the supernova Ia rate in these clusters. For this, clusters were observed using the g and r bands with MegaCam. CCCP was designed to study the scaling relations between different tracers of mass in galaxy clusters, and includes 50 clusters in the redshift range $0.15 < z < 0.55$. Of these, 20 clusters had archival *B*- and *R*-band data taken with the CFH12k camera, and 30 clusters were observed with the g and r bands with MegaCam (??).

The data were reduced using the Elixir pipeline (?), and processed further following the method outlined in ?, which is summarized below. In order to simplify point spread function (PSF) modeling for shape measurements, we homogenized the PSF across the entire field-

---

[1]We discuss sources of this discrepancy in light of recent results in

of-view by finding a locally-varying convolution kernel that makes the PSF circular and Gaussian everywhere (**?**). This PSF homogenization was done for each exposure, after which the individual exposures were co-added. By applying a Gaussian weight function to measure aperture fluxes we optimized color measurements in terms of S/N (see **?** and **?**, Appendix A). This gaussianization process introduces correlations in pixel noise, which we do not account for. As we show in Section 4.4.3, this is not a problem for the present analysis.

We performed object detection with SExtractor (**?**) in dual-image mode, using the *r* (or *R*) band as detection image. All sources were detected in the *r*-band image obtained by stacking the nonhomogenized images. Photometric zero points were calibrated using the stellar locus regression (SLR) software developed by **?**[2]. SLR uses the known colors of stars to obtain solutions for the photometric zero points of any photometric catalogue, correcting for instrumental response and atmospheric and Galactic extinctions (see also **?**). We used the Two-Micron All Sky Survey (2MASS, **?**) *J*-band star catalogue in addition to our MegaCam *g* and *r*, or CFH12k *B* and *R*, observations as inputs to the SLR. We retrieved extinction values in the *J* band from the NASA/IPAC Extragalactic Database (NED)[3], which use the reddening measurements of **?**. With these two colors, plus the absolute photometric calibrations of 2MASS (including the extinction correction), we obtained absolute zero points for the CFHT catalogues. For clusters within the SDSS footprint we also use the SDSS *griz* photometry to check for consistency, from which we conclude that SLR-corrected zero points are calibrated to an absolute uncertainty of ∼0.01 mag. Galaxies were separated from stars by visual inspection of the magnitude-size[4] plane for each cluster individually. Stars occupy a well-defined region in this plane, having essentially a single size up to the saturation flux. Given that the stacks generally have a sub-arcsecond sized PSF, galaxies used here are large compared to the PSF and are therefore easily distinguishable from stars.

We computed *r*-band absolute magnitudes, M_r, using EzGal[5] (**?**), using a passive evolution Charlot & Bruzual 2007 (unpublished, see **?**) single burst model with solar metallicity and formation redshift $z_f = 5$.

4.2.2. Spectroscopic data

We searched for spectroscopic redshifts around all clusters in the MENeaCS+CCCP sample in six archival sources: NED, the WIYN Long-Term Variability survey (WLTV; **?**), the Canadian Network for Observational Cosmology Survey (CNOC; **????**), the SDSS Data Release 10[6] (DR10; **?**) which is part of SDSS-III (**?**) and the Hectospec Cluster Survey (HeCS; **?**). We also include redshifts from the MENeaCS spectroscopic survey (hereafter MENeaCS-spec). When a galaxy was found in more than one of these catalogues, each catalogue replaced the preceding as listed above and in Table 4.1. Thus we included all redshifts from MENeaCS-spec. In NED and in SDSS DR10, we searchws for galaxies with spectroscopic redshifts within a radius of 1 deg. around each cluster, but only galaxies in our photometric catalogues were included in the analysis. From NED, we discarded all flagged redshifts (i.e., all those whose `Redshift Flag` field is not blank) and kept only redshifts with at least 4 significant digits to ensure that only spectroscopic redshifts with enough precision are included. From SDSS we only included galaxies with `zWarning=0`. The NED search includes redshifts obtained as part of large surveys such as the 2dF, the 2MASS spectroscopic

---

[2] https://code.google.com/p/big-macs-calibrate/

[3] http://ned.ipac.caltech.edu/

[4] Here, sizes are given by `FLUX_RADIUS` from SExtractor.

[5] http://www.baryons.org/ezgal/

[6] http://www.sdss3.org/dr10/data_access/

Table 4.1: Spectroscopic catalogues.

| Source	Total redshifts	Unique redshifts	Clusters	Avg. unique per cluster
		Compilations		
NED	16,125	9,161	79	116
WLTV	1,613	1,399	2	700
CNOC	1,427	1,266	10	127
SDSS DR10	14,634	13,995	62	226
HeCS	8,470	8,368	27	310
MENeaCS-spec	1,966	1,966	12	164
		Single-cluster		
?		834	1	834
?		1,115	1	1,115
Total		**38,104**	**90**	**423**

survey (2MRS), the WIde-field Nearby Galaxy cluster Survey (WINGS), and the WiggleZ Dark Energy Survey.

Additionally, we included the redshift catalogues of Abell 383 and MACS J0717.5+3745 recently published by **?** and **?**, respectively, which total 1,949 redshifts within our CFHT images. From the catalogue of **?** we used only redshifts with quality flag 1 or 2. We also highlight the redshift catalogue of Abell 2142 by **?**, containing $\sim 1{,}800$ galaxies, which is included as part of the NED catalogue.

Table 4.1 lists the number of (unique) spectroscopic redshifts included from each catalogue and from how many cluster fields they are taken. The largest redshift catalogue(s) for each cluster are listed in Table 4.2, including the largest catalogues within NED; for most clusters the NED redshifts come mainly from one or two large catalogues (with $\gtrsim 90\%$ of redshifts). The final spectroscopic sample is summarized in the last row of Table 4.1: it contains 38,104 redshifts in the direction of 90 clusters, selected to have at least 30 members, at least 10 of which must be within r_{200} (see Section 4.3.1). The left panel of Figure 4.1 shows the redshift distribution of these 90 clusters, compared to the entire MENeaCS+CCCP sample. The analysis in this paper refers only to these 90 clusters, which are listed in Table 4.2.

4.3. Galaxy samples

4.3.1. Spectroscopic members and dynamical masses
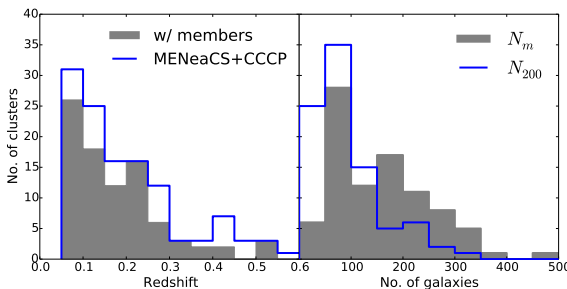
Figure 4.1: Left: redshift distributions of all ME-NeaCS+CCCP clusters (blue histogram) and clusters used in this study (gray filled histogram). Right: distributions of number of spectroscopic members, $N_{\rm m}$ (gray filled histogram), and number of spectroscopic members within r_{200}, N_{200} (blue his-
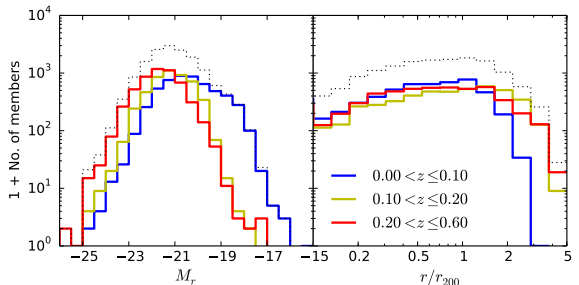
Spectroscopic membership is determined using the shifting gapper method (**?**), slightly adjusted from the implementation of **?**. We bin galaxies in radial bins of at least 15 galaxies and 250 kpc and, for each radial bin, members are selected as those galaxies that are within $800\,\mathrm{km\,s^{-1}}$ from the main body of galaxies, which is bound by gaps of $400\,\mathrm{km\,s^{-1}}$. The reduction in the velocity gaps compared to **?**—who used 1000 and 500 $\mathrm{km\,s^{-1}}$, respectively—is due to

the larger number of galaxies used here, producing a distribution that has less obvious gaps in velocity space. In some cases, we introduced a radial cut determined from visual inspection. The left panel of Figure 4.2 shows that the distribution of confirmed cluster members is similar at low and high redshift for luminous ($M_r \lesssim -21$) galaxies but low-luminosity galaxies used here come mainly from low redshift clusters.
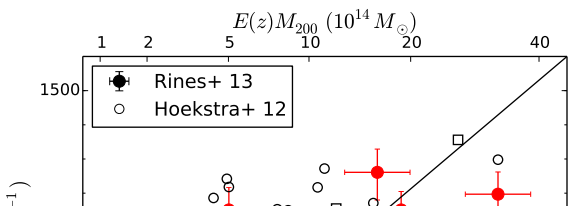
We iteratively measure the velocity dispersion, σ_{200}, as the biweight estimator of scale (**?**) using all galaxies within r_{200}, correcting for measurement errors (**?**). Since the measurement uncertainties are not available for all galaxies (most notably, they are not given in NED), we use a fiducial value of $150\,\mathrm{km\,s^{-1}}$ for the uncertainty of all redshifts, which is a conservative estimate for recent measurements, but can be representative of older or low resolution measurements listed in NED. The change in mass introduced by this correction is, in any case, at the percent level for a cluster with $\sigma \sim 1000\,\mathrm{km\,s^{-1}}$.

Figure 4.2: Distribution of spectroscopic members. Left: as a function of rest-frame absolute r-band magnitude. Right: as a function of cluster-centric distance in units of r_{200}. The dotted black lines show the distribution of the full sample; the solid lines show the distribution split into three redshift bins of approximately equal number of clusters.

The cluster redshift is determined iteratively in this process as the biweight estimator of location, considering again galaxies within r_{200}. We estimate the mass within r_{200}, namely M_{200}, using the $\sigma_{200} - M_{200}$ relation of **?**, and estimate $r_{200} = \left[3/(4\pi) \cdot M_{200}/(200\rho_c)\right]^{1/3}$. The resulting σ_{200} is insensitive to uncertainties in r_{200}; varying r_{200} by $\pm 20\%$ from those obtained from this relation only changes σ_{200} by $\lesssim 5\%$ for every cluster (in other words, velocity dispersion profiles are very close to flat near r_{200}). The uncertainties in the velocity dispersion are obtained from 1,000 jackknife samples drawn from all galaxies with peculiar velocities up to 3 times the cluster velocity dispersion; therefore quoted uncertainties include an estimate of the effect of membership selection. Uncertainties in the dynamical mass are obtained by propagating the uncertainties on the velocity dispersion. The dynamical properties described above are listed in Table 4.2, together with the number of members, N_m, and the number of members within r_{200}, N_{200}. The right panel of Figure 4.1 shows the distribution of N_{200} and N_m, the number of members out to arbitrary radius.

In cases where the spectroscopic members do not reach out to r_{200}, we cannot infer σ_{200} directly from the data. We therefore apply a correction to the measured velocity dispersion assuming the isotropic velocity dispersion profile of **?** and the mass–concentration relation of **?** to get the theoretical expectation for σ_{200} given $\sigma(< r_{max})$. This correction is linear with r_{max} for $r_{max} \gtrsim 0.2r_{200}$, with correction factors 0.93 and 0.81 for the velocity dispersion and mass, respectively, for $r_{max} = 0.6r_{200}$ (i.e., the mass

within $0.6r_{200}$ is $0.81M_{200}$), only weakly
dependent on mass and redshift. In our
sample there are 14 clusters with $r_{max} <$
r_{200}, with a median of $r_{max}/r_{200} = 0.69$
and 10th and 90th percentiles of 0.51
and 0.79, respectively. For these clus-
ters, we list the corrected values in Ta-
ble 4.2.

There are a total of 14,576 cluster
members among 90 clusters, 9,054 of
which are within r_{200}. The radial dis-
tribution of cluster members is shown
in the right panel of Figure 4.2. The
spectroscopic members on average fol-
low a Navarro-Frenk-White (NFW, **?**)
profile with concentration $c_{200} \sim 2$ (**?**).
The median redshift of the sample is $z =$
0.144, and the median velocity disper-
sion is $\sigma_{200} = 881\,\mathrm{km\,s^{-1}}$ which translates
to a median dynamical mass $M_{200} = 7.2\times$
$10^{14}\,\mathrm{M_\odot}$ and a median size $r_{200} \sim 1.7\,\mathrm{Mpc}$.
The distribution of σ_{200} is shown in the
bottom panel of Figure 4.3.

In Figure 4.3, we compare the
present velocity dispersions to those of **?**;
there is a large overlap between the two
data sets (see Table 4.1). The two sets of
measurements are consistent, with a me-
dian ratio $\langle \sigma_{200}/\sigma_{\mathrm{Rines+13}} \rangle = 1.04 \pm 0.03$.
We also show, for comparison, the singular isothermal sphere velocity dispersions fit by **?**
to the weak lensing signal of 39 overlapping clusters, which are also consistent with our
measurements to within 2% on average. It is apparent from Figure 4.3 that the agreement
between σ_{200} and σ_{WL} is better for relaxed clusters than for disturbed ones, consistent with
expectations. For comparison, using the velocity gaps used by **?** in our analysis, we obtain
velocity dispersions larger than those of **?** by ~14%.

4.3.1.1.   Dynamical state

We can take further advantage of our large spectroscopic catalogues by studying the
dynamical states of clusters. To this end we use the DS test (**?**), which uses both the positions
and velocities of galaxies. The DS test gives a measure of substructure by identifying galaxies
that do not follow the cluster velocity distribution through the metric

$$\delta^2 = \frac{N_{\mathrm{local}}}{\sigma^2} \left[(\bar{v}_{\mathrm{local}} - \bar{v})^2 + (\sigma_{\mathrm{local}} - \sigma)^2 \right]^2 , \tag{4.1}$$

where $\bar{v}_{\mathrm{local}}$ and σ_{local} are the local velocity and velocity dispersion, measured for the N_{local}
nearest neighbors around a test member, and $\bar{v}$ and σ are the global values. The Δ-statistic
is the sum of δ's over all cluster members. This statistic is then measured 5,000 times after
shuffling the velocities of cluster members, keeping positions fixed, with the same N_{local}.

Table 4.2: Cluster sample, redshifts, and velocity dispersions.

Cluster	z	N_m	N_{200}	σ_{200} (kms^{-1})	M_{200} (10^{14} M$_\odot$)	r_{200} (Mpc)	$\mathscr{S}_\Delta$	Main sources[a]	Main NED sources[b]
Abell 85	0.0555	284	248	967±55	10.0±1.7	2.03±0.12	$0.01^{+0.00}_{-0.00}$(D)	3	14
Abell 115	0.1930	73	73	1028±108	11.2±3.5	2.03±0.21	$0.24^{+0.02}_{-0.07}$(R)	—	1
Abell 119	0.0443	268	255	875±48	7.5±1.2	1.85±0.10	<0.01(D)	3	7
Abell 133	0.0558	62	59	791±79	5.5±1.7	1.66±0.17	$0.24^{+0.03}_{-0.14}$(R)	—	21
Abell 209^c	0.2090	110	110	1170±99	16.4±4.1	2.28±0.19	$0.01^{+0.00}_{-0.01}$(D)	—	27
Abell 222^c	0.2132	76	76	881±79	7.0±1.9	1.72±0.15	$0.30^{+0.04}_{-0.04}$(R)	—	11,33
Abell 223^c	0.2076	64	64	910±80	7.8±2.1	1.78±0.16	$0.05^{+0.02}_{-0.02}$(D)	—	11,33
Abell 267	0.2291	219	156	1006±74	10.3±2.3	1.95±0.14	<0.01(D)	3,4	—
Abell 383	0.1885	182	134	918±53	8.1±1.4	1.81±0.11	<0.01(D)	—	18
Abell 399	0.0718	250	229	1046±47	12.5±1.7	2.18±0.10	<0.01(D)	5	20
Abell 401	0.0735	104	83	933±81	8.9±2.3	1.94±0.17	$0.32^{+0.19}_{-0.05}$(R)	—	20
Abell 520	0.2007	153	127	1045±73	11.8±2.5	2.05±0.14	$0.27^{+0.04}_{-0.11}$(R)	—	19
Abell 521^c	0.2469	95	95	1002±95	10.1±2.9	1.92±0.18	$0.06^{+0.02}_{-0.02}$(D)	—	16
Abell 545^c	0.1577	80	80	1038±89	11.8±3.0	2.08±0.18	$0.07^{+0.00}_{-0.00}$(R)	—	2
Abell 553	0.0670	54	44	665±75	3.3±1.1	1.39±0.16	$0.01^{+0.03}_{-0.00}$(D)	5	—
Abell 586	0.1704	33	21	803±104	5.4±2.1	1.60±0.21	$0.28^{+0.12}_{-0.07}$(R)	3	—
Abell 644^c	0.0696	31	31	625±96	2.7±1.2	1.31±0.20	$0.67^{+0.11}_{-0.05}$(R)	—	24
Abell 646	0.1266	259	69	707±66	3.8±1.1	1.44±0.13	$0.07^{+0.22}_{-0.04}$(D)	3,4	—

Columns are: (1) cluster name; (2): cluster redshift; (3): number of members out to arbitrary radius; (4): number of members within r_{200}; (5): velocity dispersion of members within r_{200}; (6): total mass within r_{200}; (7): cluster radius r_{200}; (8): significance level of the DS test, the letter in parenthesis shows whether a cluster is classified as disturbed (D) or relaxed (R).

[a] Numbers are: (1): WLTV; (2): CNOC; (3): SDSS; (4): HeCS; (5): MENeaCS-spec. See text for references. [b] catalogues extracted from NED that contribute significantly to each cluster. These are: (1): ?; (2): ?; (3): ?; (4): ?; (5): ?; (6): ?; (7): WINGS (?); (8): ?; (9): 2dF (?); (10): ?; (11): ?; (12): ?; (13): WiggleZ (?); (14): ?; (15): ?; (16): ?; (17): ?; (18): ?; (19): ?; (20): ?; (21): 2MRS (?); (22): ?; (23): ?; (24): ?; (25): ?; (26): ?; (27): ?; (28): ?; (29): ?; (30): ?; (31): ?; (32): ?; (33): ?. ^{c}Spectroscopic members extend out to less than 0.8r_{200}.

Table 4.2: *Continued*

Cluster	z	$N_{\rm m}$	N_{200}	σ_{200} (km s^{-1})	M_{200} (10^{14} M$_\odot$)	r_{200} (Mpc)	$\mathscr{S}_\Delta$	Main sources[a]	Main NED sources[b]
Abell 655	0.1271	306	109	938±57	8.8±1.6	1.91±0.12	$0.03^{+0.01}_{-0.02}$(D)	3,4	–
Abell 697	0.2821	215	106	1161±89	15.4±3.6	2.19±0.17	$0.44^{+0.05}_{-0.02}$(R)	3,4	–
Abell 754	0.0546	305	300	959±43	9.8±1.3	2.01±0.09	$0.01^{+0.00}_{-0.00}$(D)	–	8
Abell 780[c]	0.0547	33	33	822±113	6.2±2.5	1.73±0.24	$0.01^{+0.01}_{-0.00}$(D)	–	21
Abell 795	0.1385	166	117	768±59	4.9±1.1	1.56±0.12	$0.06^{+0.07}_{-0.02}$(D)	3,4,5	–
Abell 851	0.4038	53	47	999±138	9.3±3.8	1.77±0.24	$0.01^{+0.03}_{-0.01}$(D)	–	3,12
Abell 959	0.2882	67	67	982±101	9.4±2.9	1.85±0.19	$0.08^{+0.04}_{-0.03}$(D)	–	5
Abell 961	0.1275	58	16	740±142	4.4±2.5	1.51±0.29	$0.84^{+0.06}_{-0.13}$(R)	3	–
Abell 963	0.2036	165	85	922±64	8.1±1.7	1.81±0.13	$0.17^{+0.06}_{-0.06}$(R)	3,4	–
Abell 990	0.1421	209	86	829±96	6.1±2.1	1.68±0.19	$0.74^{+0.05}_{-0.03}$(R)	3,4,5	–
Abell 1033	0.1224	170	98	762±52	4.8±1.0	1.56±0.11	$0.59^{+0.08}_{-0.21}$(R)	3,4	–
Abell 1068	0.1393	104	32	740±160	4.3±2.8	1.50±0.32	$0.93^{+0.04}_{-0.04}$(R)	3,4	–
Abell 1132	0.1349	160	55	727±89	4.1±1.5	1.48±0.18	$0.13^{+0.06}_{-0.05}$(R)	3,4	–
Abell 1234	0.1638	54	30	513±86	1.4±0.7	1.03±0.17	$0.87^{+0.06}_{-0.07}$(R)	3,4	–
Abell 1246	0.1920	207	87	956±84	9.1±2.4	1.89±0.17	$0.01^{+0.00}_{-0.00}$(D)	3,4	–
Abell 1285	0.1078	77	51	826±90	6.1±2.0	1.70±0.19	$0.52^{+0.08}_{-0.18}$(R)	5	–
Abell 1361	0.1157	143	46	587±62	2.2±0.7	1.21±0.13	$0.39^{+0.15}_{-0.07}$(R)	3,4	–
Abell 1413	0.1418	124	65	881±81	7.3±2.0	1.78±0.16	$0.72^{+0.07}_{-0.23}$(R)	3,4	–
Abell 1650	0.0841	266	140	720±48	4.1±0.8	1.50±0.10	$0.99^{+0.00}_{-0.02}$(R)	3,5	–
Abell 1651	0.0847	214	138	903±51	8.0±1.4	1.87±0.11	$0.65^{+0.04}_{-0.16}$(R)	–	9,21
Abell 1689	0.1847	252	235	1429±81	30.0±5.1	2.82±0.16	<0.01(D)	3,4	–
Abell 1758	0.2772	133	34	744±107	4.1±1.8	1.41±0.20	$0.11^{+0.06}_{-0.03}$(R)	3,4	–
Abell 1763	0.2323	186	103	1130±81	14.6±3.1	2.18±0.16	<0.01(D)	3,4	–
Abell 1781	0.0622	54	16	419±93	0.8±0.5	0.88±0.19	$0.92^{+0.02}_{-0.19}$(R)	3	–
Abell 1795	0.0629	191	133	778±51	5.2±1.0	1.63±0.11	$0.26^{+0.04}_{-0.09}$(R)	3	21
Abell 1835	0.2506	195	41	762±106	4.5±1.9	1.46±0.20	$0.66^{+0.06}_{-0.23}$(R)	3,4	–
Abell 1914	0.1671	257	146	911±54	7.9±1.4	1.82±0.11	$0.86^{+0.03}_{-0.05}$(R)	3,4	–
Abell 1927	0.0953	138	58	725±58	4.2±1.0	1.50±0.12	$0.25^{+0.02}_{-0.08}$(R)	3,5	–

Table 4.2: *Continued*

Cluster	z	N_m	N_{200}	σ_{200} (km s^{-1})	M_{200} ($10^{14} M_\odot$)	r_{200} (Mpc)	$\mathscr{S}_A$	Main sources[a]	Main NED sources[b]
Abell 1942	0.2257	51	27	820±140	5.6±2.9	1.59±0.27	$0.04^{+0.05}_{-0.01}$(D)	3	—
Abell 1991	0.0587	175	99	553±45	1.9±0.5	1.17±0.10	$0.12^{+0.09}_{-0.05}$(R)	3,5	—
Abell 2029	0.0777	317	181	1152±58	16.6±2.5	2.39±0.12	<0.01(D)	3	21
Abell 2033	0.0796	190	88	911±69	8.3±1.9	1.89±0.14	$0.03^{+0.03}_{-0.01}$(D)	3	21
Abell 2050	0.1202	164	82	854±80	6.7±1.9	1.74±0.16	$0.34^{+0.06}_{-0.03}$(R)	3,4	—
Abell 2055	0.1028	154	69	697±64	3.7±1.0	1.44±0.13	$0.04^{+0.02}_{-0.00}$(D)	3,4	21
Abell 2064	0.0734	62	32	675±108	3.4±1.6	1.41±0.22	$0.40^{+0.13}_{-0.05}$(R)	3	—
Abell 2065	0.0725	219	164	1095±67	14.3±2.6	2.28±0.14	$0.03^{+0.01}_{-0.01}$(D)	3	—
Abell 2069	0.1139	331	146	966±63	9.7±1.9	1.98±0.13	$0.01^{+0.00}_{-0.00}$(D)	3,4	—
Abell 2104	0.1547	90	56	1081±126	13.3±4.6	2.17±0.25	$0.22^{+0.09}_{-0.09}$(R)	—	23
Abell 2111	0.2281	256	83	738±66	4.1±1.1	1.43±0.13	$0.46^{+0.09}_{-0.04}$(R)	3,4	29
Abell 2125	0.2466	141	55	857±122	6.4±2.7	1.65±0.23	$0.46^{+0.01}_{-0.26}$(R)	—	28
Abell 2142	0.0903	1052	731	1086±31	13.9±1.2	2.24±0.06	$0.01^{+0.00}_{-0.00}$(D)	3	31
Abell 2163	0.2004	309	290	1279±53	21.5±2.7	2.51±0.10	$0.03^{+0.02}_{-0.01}$(D)	—	25
Abell 2204	0.1507	100	15	782±278	5.1±5.4	1.58±0.56	$0.35^{+0.33}_{-0.12}$(R)	—	32
Abell 2219	0.2255	364	241	1189±65	17.0±2.8	2.30±0.13	<0.01(D)	3,4	4
Abell 2259	0.1602	158	77	901±70	7.7±1.8	1.80±0.14	$0.04^{+0.12}_{-0.01}$(D)	3,4	—
Abell 2261	0.2257	206	76	882±86	7.0±2.0	1.71±0.17	$0.03^{+0.05}_{-0.02}$(D)	3,4	—
Abell 2319[c]	0.0538	83	83	1101±99	14.7±4.0	2.31±0.21	$0.52^{+0.07}_{-0.16}$(R)	—	30
Abell 2390	0.2287	136	92	1120±113	14.3±4.3	2.17±0.22	$0.23^{+0.01}_{-0.10}$(R)	2	—
Abell 2409	0.1454	101	46	826±94	6.0±2.0	1.67±0.19	$0.16^{+0.09}_{-0.03}$(R)	3,5	—
Abell 2440[c]	0.0906	88	88	766±61	4.9±1.2	1.59±0.13	$0.13^{+0.03}_{-0.02}$(R)	3	26
Abell 2495	0.0790	98	46	631±55	2.8±0.7	1.32±0.12	$0.23^{+0.06}_{-0.01}$(R)	3,5	—
Abell 2537	0.2964	175	65	909±85	7.4±2.1	1.70±0.16	$0.05^{+0.04}_{-0.01}$(D)	3	6
Abell 2597	0.0829	39	17	682±131	3.5±2.0	1.42±0.27	$0.37^{+0.15}_{-0.09}$(R)	—	9,13
Abell 2670	0.0763	241	196	919±46	8.5±1.3	1.91±0.10	<0.01(D)	3	21
Abell 2703	0.1140	75	13	657±53	3.1±0.8	1.35±0.11	$0.17^{+0.18}_{-0.05}$(R)	3	—
CL 0024.0+1652	0.3948	229	131	757±48	4.1±0.8	1.35±0.09	<0.01(D)	—	10

Table 4.2: *Continued*

Cluster	z	N_m	N_{200}	σ_{200} (km s^{-1})	M_{200} ($10^{14}\,M_\odot$)	r_{200} (Mpc)	$\mathcal{S}_\Delta$	Main sources[a]	Main NED sources[b]
MACS J0717.5+3745	0.5436	468	215	1370±79	22.0±3.8	2.24±0.13	<0.01(D)	–	15
MKW3S	0.0444	125	82	592±49	2.3±0.6	1.25±0.11	$0.83^{+0.06}_{-0.11}$(R)	3	–
MS 0015.9+1609	0.5475	232	122	1330±115	20.0±5.2	2.17±0.19	$0.32^{+0.10}_{-0.18}$(R)	1,2	–
MS 0440.5+0204	0.1962	51	35	742±103	4.3±1.8	1.46±0.20	$0.26^{+0.14}_{-0.13}$(R)	2	–
MS 0451.6−0305	0.5382	247	200	1252±55	16.8±2.2	2.05±0.09	<0.01(D)	1,2	–
MS 1008.1−1224	0.3077	86	85	1028±92	10.6±2.8	1.91±0.17	$0.59^{+0.07}_{-0.11}$(R)	2	22
MS 1224.7+2007	0.3258	33	29	790±95	4.8±1.7	1.46±0.17	$0.57^{+0.23}_{-0.07}$(R)	2,3	–
MS 1231.3+1542	0.2347	84	65	710±57	3.7±0.9	1.38±0.11	$0.87^{+0.03}_{-0.03}$(R)	2,3	–
MS 1358.4+6245	0.3289	189	152	1021±56	10.3±1.7	1.88±0.10	$0.01^{+0.01}_{-0.00}$(D)	2	17
MS 1455.0+2232	0.2565	57	57	928±111	8.0±2.9	1.77±0.21	$0.58^{+0.07}_{-0.24}$(R)	2,3	–
MS 1512.4+3647	0.3719	30	29	960±170	8.4±4.4	1.73±0.30	$0.04^{+0.03}_{-0.00}$(D)	2	–
MS 1621.5+2640	0.4254	70	41	724±82	3.5±1.2	1.27±0.14	$0.17^{+0.20}_{-0.04}$(R)	2	–
RX J0736.6+3924	0.1179	62	28	432±64	0.9±0.4	0.89±0.13	$0.52^{+0.12}_{-0.03}$(R)	3,5	–
ZwCl 0628.1+2502	0.0814	72	66	843±96	6.6±2.2	1.75±0.20	$0.04^{+0.02}_{-0.01}$(D)	5	–
ZwCl 1023.3+1257	0.1425	84	24	622±108	2.6±1.3	1.26±0.22	$0.79^{+0.17}_{-0.17}$(R)	3,4	–
ZwCl 1215.1+0400	0.0773	183	107	902±65	8.0±1.7	1.88±0.14	$0.29^{+0.02}_{-0.04}$(R)	3	–

The substructure significance (hereafter $\mathscr{S}_\Delta$) is the fraction of random samples which have Δ higher than that of the cluster. Errorbars are 68% ranges obtained from 5 runs for each cluster, varying the number of neighbors within $\sqrt{N_{200}} - 2 \le N_{local} \le \sqrt{N_{200}} + 2$, and the central value is their median. We run the DS test using only members within r_{200} because r_{200} is very close to the virial radius, beyond which the cluster *should not* be relaxed, by definition.

The DS test is not designed to assess the dynamical state of clusters in general but specifically to find substructure, which furthermore has to have a different spatial and velocity location from the cluster itself. It is therefore incomplete; there are indeed examples of known merging clusters from which the DS test cannot find indications of substructure, most notably mergers along the plane of the sky (e.g., **??**). This is the case here with Abell 520 (e.g., **?**), for example. By means of *N*-body simulations, **?** showed that $\mathscr{S}_\Delta < 0.05$ is a reasonable condition to define a pure, but not necessarily complete, sample of dynamically disturbed clusters. We follow the results of **?** in a conservative way, selecting as disturbed all cluster that are consistent with $\mathscr{S}_\Delta \le 0.05$ within errorbars (52 clusters). All others are classified as relaxed (38 clusters). This is conservative in the sense that we aim to construct a pure sample of relaxed clusters (see Section 4.5.1). Table 4.2 lists $\mathscr{S}_\Delta$ together with the classification for each cluster. We find that more massive clusters tend to be classified as disturbed (D), while less massive clusters are generally relaxed (R); this can be seen in Figure 4.3.

4.3.2. Red sequence members

While spectroscopy provides a clean sample of member galaxies from precise velocities, it suffers from incompleteness mainly due to two practical reasons: 1) obtaining a redshift for a galaxy is expensive; typically it takes ~ 30 minutes of observations for galaxies in low-redshift ($z \lesssim 0.5$) clusters, depending on the telescope and observing conditions; and 2) only a limited number of galaxies can be targeted in a single observation because of slit overlap or fiber collisions.

Being a distinct feature of clusters, the red sequence provides an ideal complement to spectroscopic members. As we show below, for luminous galaxies near the centres of clusters this also provides a clean membership selection, though not as clean as spectroscopy. Using the red sequence *in addition to* the spectroscopic selection ensures that only a small fraction of galaxies need to be included through this more uncertain method, making the purity of the sample very close to 100%.

To find the red sequence in each cluster, we first separate blue and red galaxies by fitting two one-dimensional gaussians to the color distribution of galaxies using an Error-Corrected Gaussian Mixture Model (ECGMM, **?**). We then fit a straight line in color-magnitude space to the red galaxies using a maximum likelihood approach that accounts for intrinsic scatter and the measurement uncertainty in color, iteratively rejecting 2σ outliers. Details will be presented in a forthcoming paper (Sifón et al., in prep).

We assess the purity of the red sequence as a cluster member selection procedure by looking at red sequence members that have redshifts. There are in total 57,885 red sequence galaxies up to $M_r = -17$ and within 2 Mpc, 7,224 of which have a redshift measurement ($\sim 12\%$). Figure 4.4 shows that the red sequence is a high-fidelity member selection method even to large radii. Only the sample of both low-luminosity ($M_r \gtrsim -19$) and distant ($r \gtrsim 1$ Mpc) red sequence members has a lower purity, although the latter is still $\gtrsim 70\%$ for most of this distance-luminosity space. We include in the extended sample all red sequence galaxies more luminous than $M_r = -19$ within 1 Mpc of the cluster centre. Within these parameter boundaries, 84% of red sequence galaxies with a spectroscopic redshift are confirmed cluster
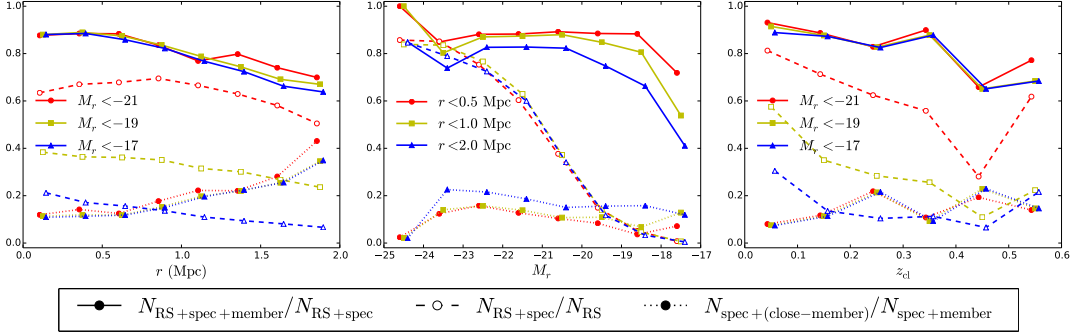
Figure 4.4: Purity of the red sequence (filled symbols with solid lines) and spectroscopic completeness within the red sequence (open symbols with dashed lines). Filled symbols with dotted lines show the fraction of galaxies that are not selected as members but that are within $\Delta z = 0.03(1+z)$ of the cluster, which represents the contamination in an unbiased photometric redshift selection. Left: as a function of cluster-centric distance, for different luminosity limits. Middle: as a function of absolute magnitude, for different radial apertures. Right: as a function of redshift for different luminosity limits, at an aperture of 1 Mpc. Note that points within a given line are independent (each line is a differential distribution), but lines of the same type are not independent from each other.
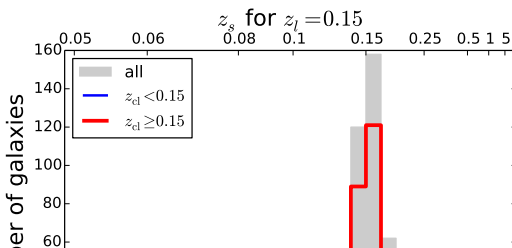
members. This level of contamination (16% of red sequence members) has no effects on our results.

The rightmost panel of Figure 4.4 shows that up to $z \sim 0.4$, the purity is extremely high ($\sim$90%) but then decreases to $\sim$70%, because above $z \sim 0.4$ the 4000Å break is no longer bracketed by the *g* and *r* bands (similarly for the *B* and *R* bands). The completeness of the spectroscopic samples does drop noticeably with redshift because of the higher difficulty posed by spectroscopic observations of high redshift clusters.

From a lensing perspective, one other important ingredient in assessing the red sequence is the redshift distribution of the contaminating fraction, which we can quantify using red sequence galaxies that are confirmed to be outside the cluster. If they are sufficiently far behind the cluster, they could in fact be lensed, inducing a signal that we wish to avoid. If instead they are either very close behind or in front of the cluster, then they will not be lensed and will only dilute the signal. Figure 4.5 shows the redshift distribution of red sequence galaxies that are confirmed to be nonmembers through the distance ratio, D_{ls}/D_s, where D_{ls} is the angular diameter distance between the lens (i.e., cluster) and the source galaxy, and D_s is the angular diameter distance to the source. Note that $D_{ls} < 0$ for $z_s < z_l$. Galaxies behind the clusters are lensed, resulting in (apparent) tangential alignments. The amplitude of this effect can be quantified by the "lensing efficiency," β, defined as

$$\beta \equiv \left\langle \max\left(0, \frac{D_{ls}}{D_s}\right) \right\rangle, \tag{4.2}$$

which is typically calculated using photometric redshifts or an average redshift distribution. Note that Equation 4.2 naturally accounts for galaxies in front of the cluster, which do not contain a lensing signal (but do introduce noise), which is especially important when using a generic redshift distribution, or full photometric redshift probability distributions (in which case background galaxies have a nonzero probability of being in front

of the cluster). Of the 688 confirmed non-members in the red sequence, 496 (72%) are behind the cluster (incuding those immediately behind the cluster), and the lensing efficiency of red sequence nonmembers is $\beta = 0.085$. It is therefore possible that the contaminating red sequence galaxies contain some lensing signal from background galaxies, but within the red sequence selection limits imposed here, this sample is only 16% of the red sequence galaxies. Therefore there is a fraction $\sim 0.72 \times 0.16 \simeq 12\%$ of contaminating galaxies (with $\sim 0.28 \times 0.16 \simeq 4\%$—those in the foreground—adding noise). The lensing signal in these galaxies is $\gamma_{+,\mathrm{rs}} \lesssim 0.11 \cdot \beta \cdot \gamma_+ = 0.11 \cdot 0.085 \cdot 0.10 \approx$ 9×10^{-4}, several times smaller than the statistical uncertainties (where $\gamma_+ \approx 0.1$ is a typical shear amplitude in the inner regions of galaxy clusters).

In summary, the red sequence gives a high-fidelity cluster member selection. It is important, however, to restrict this selection to the inner regions of clusters and to luminous galaxies (as shown in Figure 4.4), because the red sequence may contain some lensing signal. The purity of the red sequence as selected here is 84%, so this contamination is not expected to be significant. Adding the red sequence members to the 14,576 spectroscopically confirmed members gives a total of $N_{\mathrm{m}} + N_{\mathrm{rs}} = 23{,}041$ members with an estimated contamination of $0.16 \cdot N_{\mathrm{rs}} / (N_{\mathrm{m}} + N_{\mathrm{rs}}) \approx 8\%$.

4.3.3. Photometric redshift contamination

By taking a fixed width in velocity, we can simulate the members found by an accurate, unbiased photometric redshift criterion. The dotted lines in Figure 4.4 show the fraction of galaxies that are within $\Delta z = 0.03(1 + z)$ (as expected for large ongoing photometric redshifts) but are not members of the cluster,[7] as determined in Section 4.3.1. The contamination is roughly independent of magnitude at all radii and at a level of $\sim 13\%$ within 1 Mpc of the BCG, rising steeply beyond this radius. In terms of apparent magnitude the curves look similar in the range $m_r \lesssim 23$, the range in which most of the selected red sequence galaxies are found. This contamination rises shallowly with redshift, reaching $\sim 20\%$ at $z \gtrsim 0.3$.

The radial dependence in Figure 4.4 is shown in physical units instead of in units of r_{200} because this is more generally used with photometric surveys where the physical size of each cluster is not known, and Figure 4.4 gives an idea of the apertures that should be used to either search for clusters or characterize the cluster based on a red sequence sample.

Comparing the dotted and solid curves, it seems that there is not such a significant gain in using photo-z's versus the red sequence. A photo-z selection has the advantage that it selects a more representative population of the cluster, and that the red sequence depends on a single color (at least in this implementation) and it becomes less reliable when the 4000Å break is not bracketed by the filters used. This is the case in our study for $z \gtrsim 0.36$. It is also apparent, as with the red sequence, that a photo-z selection becomes significantly contaminated beyond $r \sim 1\,\mathrm{Mpc}$.

---

[7] $\Delta z = 0.03(1 + z)$ corresponds to $\approx 10{,}000\,\mathrm{km\,s^{-1}}$ at the median redshift of the sample, $z = 0.15$.

Finally, we note that the galaxies we refer to here (shown with the dotted lines) are not cluster members but also do not contribute a lensing signal, because they are too close behind. They are, indeed, likely to be part of the same large-scale structure of the cluster so would probably feel tidal torque from it similar to the actual member galaxies. Thus from the perspective of galaxy alignment measurements these galaxies should not dilute the signal significantly, nor introduce a lensing signal.

4.3.4. Control samples

We construct two catalogues as control samples to assess spurious contributions to our measurements. The shapes of objects in these two samples are unaffected by the cluster (and are mostly unrelated between objects in each sample), so their alignment signals (see Section 4.4) should be consistent with zero. A departure from zero would mean that there is significant residual PSF ellipticity in the images, and therefore that the shape measurements are unreliable.

First, we use all stars in the magnitude range $17 < m_r < 22$, selected as outlined in Section 4.2.1, for a total of 443,321 stars. We choose the bright limit to avoid saturated stars, whereas the faint limit ensures that the star sample is not contaminated by faint, unresolved galaxies.

We also use all spectroscopically confirmed foreground galaxies, which are selected as all galaxies with peculiar velocities more negative than $-10{,}000\,\mathrm{km\,s^{-1}}$ in the rest-frame of the cluster. There are 3,666 spectroscopically confirmed foreground galaxies in the direction of 73 clusters. The clusters with the most foreground galaxies are two high-redshift clusters, namely MS 0451.6−0305 at $z = 0.539$ and MACS J0717.5+3745 at $z = 0.544$, with $N_{\mathrm{fg}} = 306$ and $N_{\mathrm{fg}} = 304$, respectively.

4.4. Measuring intrinsic alignments

We measure the alignment signal of galaxies within clusters by weight-averaging the ellipticity components of all galaxies within a given radial annulus,

$$\langle \epsilon_i \rangle = \frac{\sum_n w_n \epsilon_{i,n}}{\sum_n w_n} \,, \tag{4.3}$$

with weights equal to

$$w_n = \frac{1}{\epsilon_{\mathrm{int}}^2 + \sigma_n^2} \,, \tag{4.4}$$

where σ_n is the measurement uncertainty on the ellipticity of the n-th galaxy. We assume an intrinsic (i.e., unlensed) galaxy ellipticity dispersion $\epsilon_{\mathrm{int}} = \sqrt{\langle \epsilon_i \epsilon_i \rangle} = 0.25$. The uncertainty in Equation 4.3 is equal for both components and is given by $\sigma(\epsilon_i) = \left(\sum_n w_n \right)^{-1/2}$. In this work, we use the shapes of cluster members to measure three kinds of alignment: the alignment of (satellite) galaxies toward the centre of the cluster, the alignment of galaxies with respect to the BCG orientation, and the alignment between satellite galaxies. These three quantities are detailed below.

Throughout, we refer to raw ellipticities as e_i, and to ellipticities that account for instrumental effects (i.e., PSF size in the case of gaussianized images) as ϵ_i.

4.4.1.   Different alignment signals

In this section we outline the different rotations we apply to the ellipticity measurements of Section 4.4.2 in order to extract alignment signals within clusters.

4.4.1.1.   Satellite radial alignment

We measure the alignment of galaxies with respect to the centre of the cluster using ellipticity components rotated to a frame such that

$$\epsilon_+ = -(\epsilon_1 \cos 2\theta + \epsilon_2 \sin 2\theta) \tag{4.5}$$

$$\epsilon_\times = \epsilon_1 \sin 2\theta - \epsilon_2 \cos 2\theta \tag{4.6}$$

where ϵ_1 and ϵ_2 are the galaxy ellipticities in the cartesian frame, with ϵ_1 measuring the ellipticity in the x and y directions, and ϵ_2 in diagonal directions. Here θ is the azimuthal angle with respect to the centre of the cluster. In this frame, ϵ_+ measures the distortion in the tangential and radial directions while $\epsilon_\times$ measures the distortion at $\pm 45°$ from the radial direction (see, e.g., Figure 1 of **?**, for a diagram). Note that the definition of ϵ_+ in Equation 4.5 has the opposite sign to that typically used in weak lensing analyses. For symmetry reasons the cross component, $\langle \epsilon_\times \rangle$, of an ensemble of clusters should be consistent with zero (although a single cluster might have a preferred nonradial alignment direction such that $\langle \epsilon_\times \rangle \neq 0$, the average over an ensemble of clusters must be zero), so it serves as a check for systematic effects. On the other hand, $\langle \epsilon_+ \rangle < 0$ indicates that galaxies are preferentially aligned in the tangential direction, as is the case for gravitationally lensed background galaxies, while $\langle \epsilon_+ \rangle > 0$ would indicate a radial alignment of the galaxies, which could be the case for cluster members. Finally, $\langle \epsilon_+ \rangle = 0$ implies that galaxies are randomly oriented toward the centre of the cluster.

4.4.1.2.   Satellite-BCG alignment

To measure the alignment between satellite galaxies and the BCG, we rotate the shapes and coordinates of satellites to a frame where the direction of $\epsilon_1 > 0$ coincides with the major axis of the BCG, namely

$$\begin{aligned} \epsilon_1' &= \epsilon \cos\left[2\left(\phi - \phi_{\mathrm{BCG}}\right)\right] \\ \epsilon_2' &= \epsilon \sin\left[2\left(\phi - \phi_{\mathrm{BCG}}\right)\right], \end{aligned} \tag{4.7}$$

where ϕ and ϕ_{BCG} are the position angles of a satellite galaxy and the BCG, respectively, and $\epsilon \equiv (\epsilon_1^2 + \epsilon_2^2)^{1/2}$ is the ellipticity of the galaxy. In this new frame, the BCG has ellipticity components $\epsilon_1' = \epsilon$ and $\epsilon_2' = 0$. For the BCG position angles we use only GALFIT measurements (see Section 4.4.2.2), since these are expected to be more reliable for galaxies as large as BCGs. Analogous to the radial alignments, $\langle \epsilon_1' \rangle > 0$ implies that satellite galaxies are oriented along the major axis of the BCG, $\langle \epsilon_1' \rangle < 0$ that satellites are oriented along the BCG minor axis, and $\langle \epsilon_1' \rangle = 0$ implies random orientations; ϵ_2' measures diagonal alignments so we expect $\langle \epsilon_2' \rangle = 0$.

4.4.1.3.   Satellite-satellite alignment

Finally, we compute the alignment between satellite galaxies within clusters by calculating Equation 4.5 taking every satellite galaxy as a test galaxy (i.e., as the frame for θ). BCGs are

excluded from this analysis. This probes potential alignments of galaxies in substructures within the cluster. In principle, if there are N members in a cluster, the number of pairs is equal to $N(N-1)/2$. However, we only use pairs for which a full circle can be averaged, to avoid averages that include mostly objects in the corners of the images where PSF residuals may be larger. This is a concern for massive, low redshift clusters, where $30'$ (half the side of the MegaCam image) is roughly equal to r_{200} in the worst cases. To ensure that the average remains unbiased, therefore, we only include pairs such that the sum of the distance between the test galaxy and the centre of the cluster and the separation between the two satellites is less than 90% of the distance between the cluster centre and the edge of the image.

4.4.2. Shape measurements

Measuring galaxy shapes is a challenging endeavor, especially in the presence of noise and PSF anisotropies (e.g., **???**). For large (in units of the PSF), bright objects such as those used here, this should be less of a problem. Moreover, after gaussianization the PSF ellipticity is negligible. In this work we measure the shapes of member galaxies using two different methods, which allows us to test for consistency and robustness of the results. Below we give a brief outline of each method to highlight their differences; more details can be found in the original works.

Shapes are measured from the gaussianized images (Section 4.2.1). The PSF in these images is, by construction, circular, gaussian, and constant across the image. Therefore the shape measurement methods need to account for the blurring of the ellipticity by the PSF, but there are no systematic ellipticities in the images (to a high enough precision, see Section 4.4.3).

4.4.2.1. Kaiser-Squires-Broadhurst (KSB)

KSB was developed for weak lensing measurements by **?** and revised by **?**. It measures shapes by estimating the central second moments I_{ij} of the image fluxes to measure the two-component polarization

$$e_1 = \frac{I_{11} - I_{22}}{I_{11} + I_{22}} \, ; \; e_2 = \frac{2I_{12}}{I_{11} + I_{22}} \, . \tag{4.8}$$

These measurents are weighted with a circular Gaussian of width r_g, which corresponds to the radius of maximum significance measured by KSB; this weight reduces shot noise in the measurements. Blurring by the PSF is corrected by the so-called pre-seeing shear polarizability, P^γ, which quantifies the effect of the convolution of the PSF to the image polarization, e_i (**??**). The corrected ellipticity is then $\epsilon_i = e_i/P^\gamma$.[8] Both e_i and P^γ are measured with the same radius, r_g, for each galaxy.

4.4.2.2. GALFIT

GALFIT was developed by **?**, having in mind the modeling of different components of galaxies for studies of galaxy structure and evolution. It attempts to model the light of a galaxy by fitting a multi-component generalized ellipse given by

$$r = \left(|x|^{c+2} + \left| \frac{y}{q} \right|^{c+2} \right)^{1/(c+2)} \tag{4.9}$$

---

[8]Because the PSF in our images has vanishing ellipticity by construction, the PSF correction of KSB is mathematically exact. This is not the case if the PSF is significantly elliptical.

where a true ellipse has $c = 0$, a boxy shape $c > 0$ and a disky shape $c < 0$; here q is the minor-to-major axes ratio. Additionally, the position angle, ϕ, is defined as the direction of the major axis. GALFIT accounts for the PSF model (in this case a single gaussian for each whole field) when measuring ellipticities. We use a simple **?** model for the surface brightness profile, $\ln I(r) \propto r^{1/n}$. Only galaxies with Sérsic index $0.5 < n < 8$ and with axis ratio $q > 0.15$ are included in the sample. We convert q and ϕ to the same ellipticity measures of KSB through

$$\epsilon_1 = \left(\frac{1-q}{1+q}\right)\cos 2\phi; \; \epsilon_2 = \left(\frac{1-q}{1+q}\right)\sin 2\phi. \tag{4.10}$$

4.4.3. Systematic effects

Because weak lensing measurements rely on averages of a large number of small signals, they are more prone to systematic effects than photometry and require more agressive masks. Therefore some spectroscopic members (all of which are in our photometric catalogue) are not included in the shape catalogues. Moreover, the KSB and GALFIT catalogues are not the same since both have different requirements on, e.g., the size of an object and blending with nearby objects to estimate a reliable shape. Of the 14,576 spectroscopic members, 13,966 have a KSB shape measurement and 13,360 have a GALFIT measurement, with an overlap of 12,160 galaxies and a total of 14,250 galaxies with a shape measurement. Similarly, of 23,041 spectroscopic+RS members, 20,493 have KSB measurements and 18,511 have GALFIT measurements. The smaller number of objects with GALFIT measurements comes mainly from high-redshift galaxies (compare Tables 4.3 and 4.4). This is because small, faint galaxies are harder for GALFIT to fit, while KSB is well-suited to measure the shapes of faint (background) galaxies.
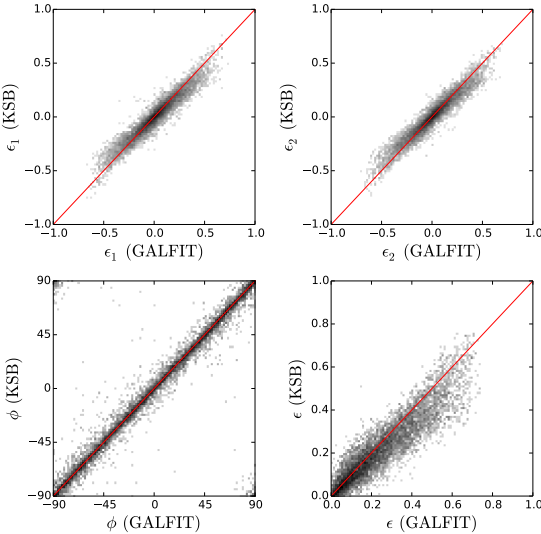
Figure 4.6: Comparison of shape measurements from KSB and GALFIT. Grey scales show the number of points per bin in logarithmic scale. Red lines show $y = x$. Top: Ellipticity components in cartesian coordinates. Bottom left: position angles, ϕ, in degrees. The periodicity of ϕ (of 180 deg) can be seen in the top left and bottom right corners of the plot. Bottom right: galaxy ellipticities.

We only consider galaxies with shape measurements from either method in this work, except for the assessment of the red sequence in Section 4.3.2. Figure 4.6 compares the shape parameters for all spectroscopic members that have valid KSB and GALFIT estimates. While the measurements generally agree, there is a small but noticeable difference for large-ellipticity objects, such that KSB estimates lower ellipticities than GALFIT. This effect is present with more or less the same magnitude for all clusters; it is a genuine difference between the two methods (for our particular dataset), and there is an indication that this effect may be more pronounced for smaller objects. This difference is due to higher-order corrections that are not implemented in KSB, which become important at large ellipticities (**?**). As we show in Section 4.5 this has no impact on our results, so we do not explore this issue further.

As a further test, Figure 4.7 shows the alignment signals of the control samples. As
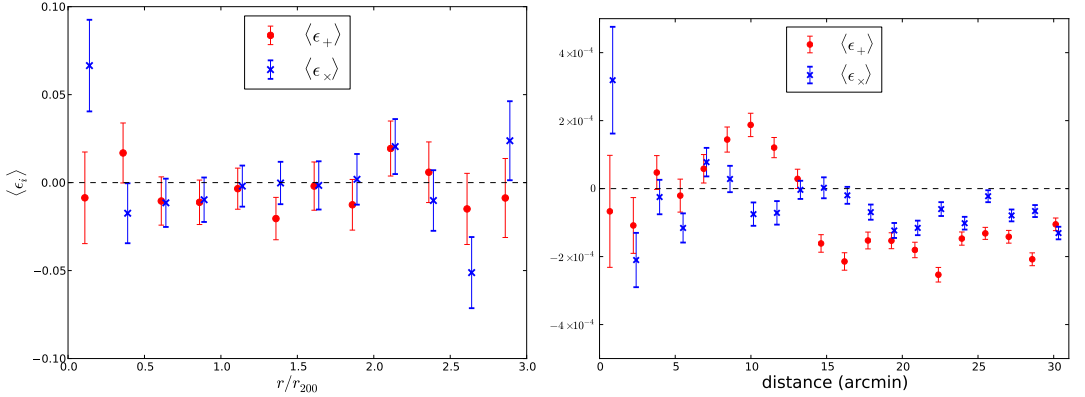
Figure 4.7: Alignment signal from control samples measured with KSB, with data points shifted horizontally for clarity. Left: 3,666 foreground galaxies in the direction of 73 clusters as a function of distance from the cluster, in units of r_{200}. Right: stars in the magnitude range $17 < m_r < 22$ as a function of angular distance from the centre of each cluster. Typically, $r_{200} \sim 10'$. Note the different vertical scales in each plot.

expected, foreground galaxies have a signal consistent with zero in both ellipticity components at all radii, with large errorbars due to small statistics. The average ellipticities of stars are different from zero at significant levels in most of the radial range. However, the average ellipticity is constrained to $\langle \epsilon_i \rangle \lesssim 2 \times 10^{-4}$ at all radii, an order of magnitude smaller than the statistical errors in the alignments of cluster members. Thus any systematic effects arising from PSF uncertainty or other instrumental biases are controlled to much lower values than the statistical uncertainties, and can be neglected for the purposes of this work.

Finally, the gaussianization of the images makes the PSF round and homogeneous across an image but produces anisotropic (correlated) noise, which could introduce noise bias in our measurements. The level of anisotropy can be assessed by measuring star ellipticities as a function of magnitude: if noise is highly anisotropic then noisier measurements would show, on average, a larger anisotropy than high-S/N measurements. We test this by comparing the ellipticities of stars as a function of magnitude (for $18 \leq m_r \leq 22$), and find that the average ellipticities are consistent with the levels shown in Figure 4.7. Moreover, we use galaxies whose number density drops rapidly beyond $m_r \sim 18$, and are typically 8 times larger than the PSF. We conclude that anisotropic noise can be safely neglected in this study.

4.5. Results

In this section we present and discuss the main results of this paper. We refer to Section 4.4 for details on the calculations that lead to the values reported here and a discussion of systematic effects.

4.5.1. Satellite radial alignment

Figure 4.8 shows the average radial alignment for all spectroscopically confirmed cluster members with good ellipticity measurements from KSB and GALFIT in annuli around the cluster centre. Both methods show that the intrinsic alignment signal of cluster members

is consistent with zero across all radii. Hereafter, we choose to quote average values within r_{200} since, strictly speaking, this is the input required by the halo model (see Section 4.6). Within r_{200}, the alignment of spectroscopic members is constrained to an average of $\langle \epsilon_+ \rangle = -0.0037 \pm 0.0027$ with KSB and $\langle \epsilon_+ \rangle = 0.0004 \pm 0.0031$ with GALFIT at 68% confidence. The cross components are also consistent with zero. Including red sequence members roughly doubles the number of galaxies used and confirms the latter result, with $\langle \epsilon_+ \rangle = -0.0022 \pm 0.0020$ and $\langle \epsilon_+ \rangle = 0.0000 \pm 0.0026$ with KSB and GALFIT, respectively.

Our results are consistent with the nondetection of satellite radial alignments in massive clusters at $z > 0.5$ (?), based on ~ 500 spectroscopic members in the inner ~ 500 kpc of clusters, using imaging from the Hubble Space Telescope (HST), and also with measurements at smaller masses from photometrically-selected galaxy groups from SDSS (??) and spectroscopically-selected galaxy groups from the Galaxy And Mass Assembly (GAMA) survey (?). Our results suggest that the stars in galaxies within clusters do not feel a strong enough tidal torque to be aligned toward the centre of the cluster, in contrast with results from simulations which find strong alignments even when accounting for differences in the response between stars and dark matter which naturally occurs in hydrodynamical simulations (??, Velliscig et al. in prep). An obvious consideration from the observational point of view is miscentring: whether the chosen cluster centre is really the minimum of the cluster potential. This effect can be measured statistically with stacked weak lensing measurements (e.g., ?) but is otherwise hard to assess observationally. At least in very relaxed clusters, BCGs are typically very close to the peak of the gas distribution (e.g., ??), which is closely matched to the dark matter distribution (?). We can therefore test, to some extent, whether miscentring could be diluting an alignment signal by isolating relaxed clusters as discussed in Section 4.3.1.1. However, as shown in the top-left panel of Figure 4.9, we do not detect any alignment signal neither from relaxed nor from disturbed clusters. Thus we conclude that our results are robust to miscentring effects and that, statistically, satellite galaxies do not align toward the centres of clusters.

As discussed by ?, the redshift evolution of satellite radial alignments (or lack thereof) contains valuable information as to whether these alignments are produced during the formation of clusters or an evolving product of tidal torques within clusters. The centre-left panel of Figure 4.9 shows that the alignment signal is consistent with zero across redshift, suggesting that neither of these processes is sufficient to sustain radial alignments over cosmological time. Furthermore, the bottom-left panel of Figure 4.9 shows that this nondetection is also independent of cluster mass. We further tested whether any orientation bias, in the sense that we might have clusters viewed preferentially along their major axis, could have any effects on our results. To do this, we divided the cluster sample by BCG elongation, assuming that BCGs that look rounder might actually be elongated along the line-of-sight. Both cluster samples have radial alignments consistent with zero (not shown), arguing that a possible orientation bias is not a problem here.

In any of the two scenarios mentioned above (namely tidal and primordial alignments), radial alignments could show a different pattern for galaxies with different formation histories. We investigate this by splitting the galaxy sample by galaxy luminosity (as a proxy for galaxy mass) and color—since bluer galaxies have been accreted more recently. To split by galaxy color we use each cluster's red sequence, which depends linearly on apparent magnitude, as outlined in Section 4.3.2. As seen in the right panels of Figure 4.9, we find no radial alignments consistently across galaxy colors and luminosities.

The results discussed above are summarized in Tables 4.3 and 4.4 for spectroscopic and spectroscopic plus red sequence member samples, respectively.

Table 4.3: Average ellipticity components of spectroscopic members.

Sample	KSB				GALFIT			
	$N_{gal}{}^{a}$	$\langle\epsilon_+\rangle$	$\langle\epsilon_\times\rangle$	$\sigma(\epsilon_i)^{b}$	$N_{gal}{}^{a}$	$\langle\epsilon_+\rangle$	$\langle\epsilon_\times\rangle$	$\sigma(\epsilon_i)^{b}$
All	8,510	−0.0037	−0.0014	0.0027	8,014	0.0004	−0.0009	0.0031
$z < 0.14$	4,170	0.0002	−0.0000	0.0039	4,612	0.0029	−0.0003	0.0038
$z \geq 0.14$	4,340	−0.0074	−0.0027	0.0038	3,402	−0.0042	−0.0020	0.0053
$M_{200} < 7 \times 10^{14} M_\odot$	2,287	−0.0059	0.0051	0.0052	2,277	−0.0057	0.0041	0.0057
$M_{200} \geq 7 \times 10^{14} M_\odot$	6,223	−0.0029	−0.0038	0.0032	5,737	0.0030	−0.0030	0.0037
Relaxed	3,233	−0.0037	−0.0022	0.0044	3,058	−0.0038	−0.0025	0.0050
Disturbed	5,277	−0.0036	−0.0009	0.0034	4,956	0.0031	0.0001	0.0040
$M_r \leq -21$	4,101	−0.0031	−0.0016	0.0039	3,922	0.0009	−0.0000	0.0044
$M_r > -21$	4,409	−0.0042	−0.0012	0.0038	4,092	−0.0001	−0.0018	0.0044
RS	5,806	−0.0008	−0.0009	0.0033	5,595	0.0010	−0.0001	0.0037
Non-RS	2,704	−0.0099	−0.0025	0.0048	2,419	−0.0012	−0.0031	0.0059

[a]Number of galaxies used for the average, within r_{200}. [b]68% confidence measurement uncertainties on the average ellipticities.

Table 4.4: Average ellipticity components of spectroscopic plus red sequence members.

| Sample	KSB				GALFIT			
	N_{gal}	$\langle\epsilon_+\rangle$	$\langle\epsilon_\times\rangle$	$\sigma(\epsilon_i)$	N_{gal}	$\langle\epsilon_+\rangle$	$\langle\epsilon_\times\rangle$	$\sigma(\epsilon_i)$
All	15,905	−0.0022	−0.0021	0.0020	12,930	0.0000	−0.0008	0.0026
$z < 0.14$	6,407	−0.0020	−0.0019	0.0031	6,233	0.0013	0.0002	0.0033
$z \geq 0.14$	9,498	−0.0023	−0.0022	0.0026	6,697	−0.0019	−0.0023	0.0041
$M_{200} < 7 \times 10^{14} \mathrm{M}_\odot$	5,394	−0.0039	−0.0010	0.0034	4,345	−0.0057	0.0009	0.0044
$M_{200} \geq 7 \times 10^{14} \mathrm{M}_\odot$	10,511	−0.0013	−0.0027	0.0024	8,585	0.0031	−0.0017	0.0032
Relaxed	7,504	−0.0034	−0.0051	0.0029	5,903	−0.0044	−0.0038	0.0038
Disturbed	8,401	−0.0011	0.0006	0.0027	7,027	0.0039	0.0018	0.0035
$M_r \leq -21$	5,394	−0.0020	−0.0011	0.0034	4,912	0.0008	0.0004	0.0040
$M_r > -21$	10,511	−0.0023	−0.0026	0.0024	8,018	−0.0005	−0.0017	0.0034

4.5.2. Satellite-BCG alignment

The second type of alignment we explore is the alignment of the satellite orientations with the BCG orientation (cf. Equation 4.7). A large number of observations suggest that BCGs are on average oriented along the major axes of clusters themselves (e.g., **?????**), and there is evidence that the velocity dispersion of satellite galaxies is typically larger along the BCG major axis (**?**). It is possible, then, that the BCG orientation represents a preferred infall direction. If this is the case, it is possible that galaxies would be aligned toward this infall direction.

Figure 4.10 shows the alignment of galaxies with the major axis of the BCGs measured with KSB as a function of radius, for the full sample of spectroscopic plus red sequence members. As in the case of radial alignments, the data are also consistent with no satellite-BCG alignments at all distances. The average KSB signal within r_{200} is $\langle \epsilon'_1 \rangle = -0.0021 \pm 0.0022$; the average GALFIT
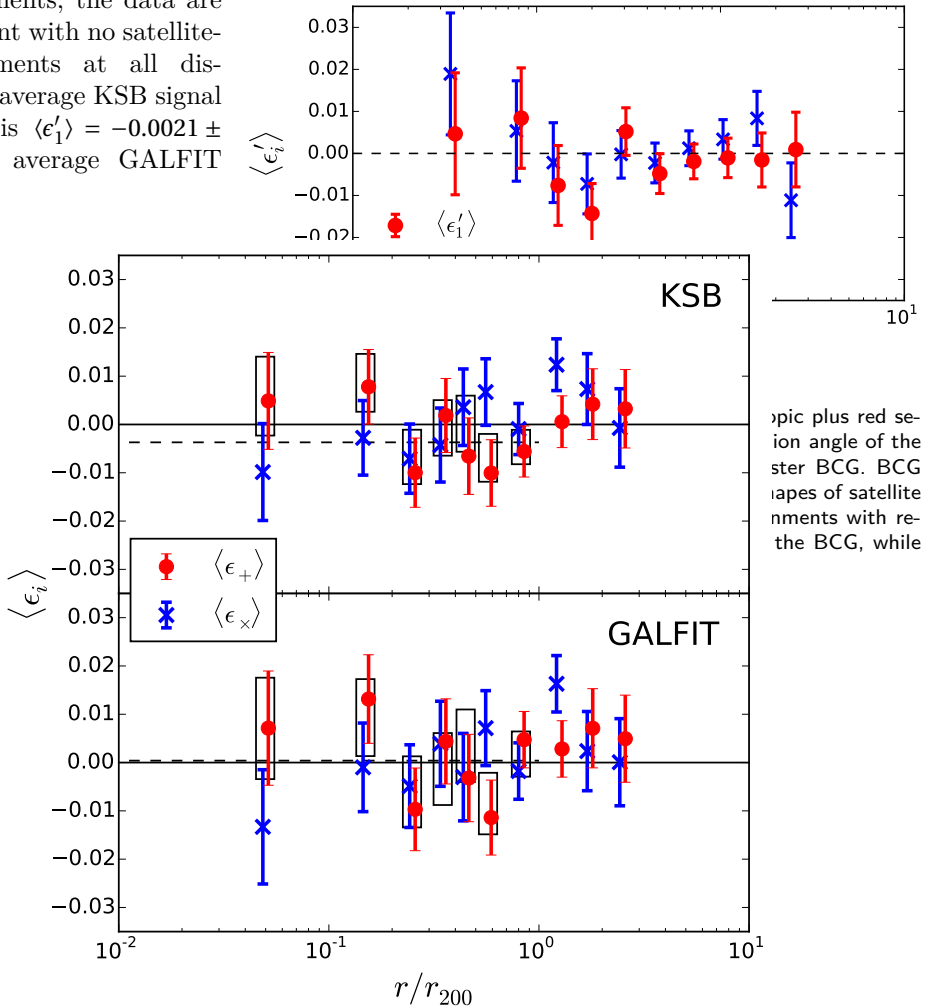
Figure 4.8: Average alignment of all spectroscopically confirmed members out to $3r_{200}$. The top panel shows the results from KSB while the bottom panel shows those from GALFIT. Shaded bands show the 1, 2 and 3σ uncertainties in the overall average and white bars show the 1σ range for $\langle \epsilon_+ \rangle$ from the enhanced sample including red sequence members. Points are slightly shifted horizontally for clarity.
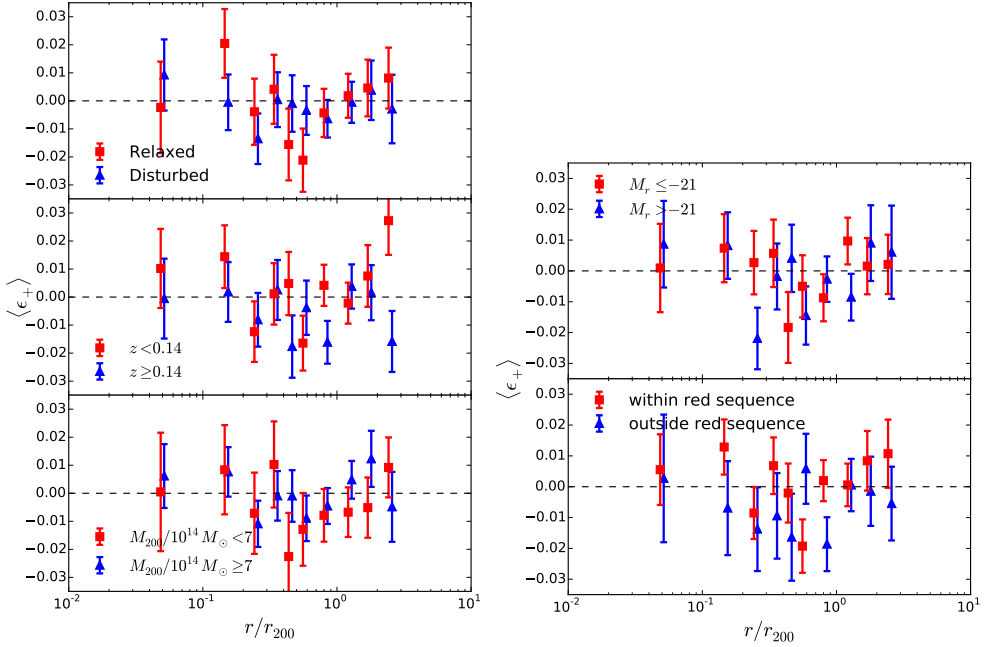
Figure 4.9: Average alignment $\langle \epsilon_+ \rangle$ from KSB for spectroscopically confirmed members, divided by cluster properties (left): by dynamical state (top; see Section 4.3.1.1), redshift (middle), and dynamical mass (bottom), and by galaxy properties (right): by rest-frame r-band absolute magnitude (top) and colour with respect to the red sequence (bottom).

signal is $\langle \epsilon_1' \rangle = -0.0024 \pm 0.0029$. We also split the sample as in the preceeding section, and find no signal for all galaxy and cluster subsamples. As a consistency check, we also find that the distribution of position angles, $|\phi - \phi_{\mathrm{BCG}}|$, is consistent with a random distribution.

Finally, we averaged not in annular bins but in cartesian coordinates $\{x, y\}$, to check if the satellite-BCG alignment could be happening only along a preferential direction, such that the azimuthal average would dilute the signal. We also found a null signal in this case (not shown).

4.5.3. Satellite-satellite alignment

We have shown in Section 4.5.1 that satellite galaxies are not aligned toward the centres of clusters. If galaxies reside within substructures themselves, then these substructures might have tidally aligned galaxies toward them. If the tidal torque of the cluster is not enough
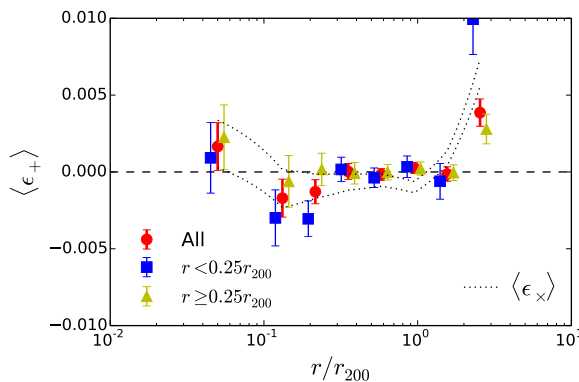
to overcome these substructure-scale alignments, then maybe we can observe an alignment signal at small separations, between satellite galaxies. After excluding data near the edges of the images (see Section 4.4.1.3), we use a total of 3.93×10^6 satellite pairs. Figure 4.11 shows the alignment signal between satellites averaged over all clusters, as a function of distance between satellites, for the full spectroscopic plus red sequence member sample. In this case we split the sample into two radial bins, namely (test) galaxies within and outside $0.25r_{200}$, which corresponds to the scale radius of a cluster with a concentration $c_{200} = 4$ (roughly what is expected for massive clusters; e.g., **?**), but the results are similar when splitting the sample at other radii.

The leftmost bins in Figure 4.11 show the signal from substructure: outer bins probe the radial alignment between galaxies at large distances. It might be expected that substructure in the outskirts of clusters would contain an alignment signal since, presumably, they have been accreted more recently. As in the preceeding sections, we do not observe any alignment signal for the full cluster sample, nor for relaxed or disturbed clusters, at any radii. We note however that the last data point in Figure 4.11 is significantly nonzero, but so is the cross component. This suggests that at these distances measurements are affected by systematic effects, mainly because a large fraction of the pairs consist of two galaxies at the edges of the images. Moreover, this data point shows the alignments between satellites at opposite sides of the cluster; i.e., it is not a measurement of alignment within cluster substructure.

Since we do not detect any alignment signal for clusters at different redshifts and at different dynamical stages, we conclude that tidal torques in clusters, or in substructures within them, do not result in significant alignments of the stellar content of galaxies at any scale (neither toward the centre nor between galaxies). It may be possible to bring this in line with the strong alignments measured in *N*-body simulations by invoking a misalignment between the stellar and dark matter distributions (e.g., **??**). However, such analysis is beyond the scope of this paper.

4.5.4. Is there an agreement on the level of galaxy alignments in groups and clusters?

As discussed above, previous studies have reported various levels of alignment of satellite galaxies in clusters using different estimators. We expect such a lack of agreement to arise for two main reasons: the quality of the images used to measure galaxy shape parameters, and the use of shape measurements that are prone to systematic effects, e.g., isophotal measurements.

The latter effect was studied by **?** in detail; they found significant radial alignments only when using isophotal shape measurements, and that the strength of these alignments depends on apparent magnitude but *not* on absolute magnitude, a strong suggestion that the detection is an artifact. Specifically, isophotal measurements are subject to severe contamination from the BCG, which can extend over a few hundred kpc in the case of massive clusters. As to the first cause, the quality of imaging data used by different groups varies significantly.

Figure 4.11: Satellite-satellite alignment as a function of the distance between satellites, for the full spectroscopic plus red sequence member sample. Red circles show all galaxies, while blue squares and yellow triangles show the signal with respect

To our knowledge, **?** were the first to use CCD photometry to measure galaxy alignments. They found a significant anisotropy in the (isophotal) position angles of satellite galaxies of Abell 521 (though they used photographic plates for their statistical study of alignments in clusters). There are also recent studies, however, who used position angle measurements extracted from scanned photographic plates (e.g., **???**), both of which are of noticeably lower quality than present-day observations. Moreover, these works typically used single-band information to select cluster members, yielding an unknown (and likely low) sample purity.

Most recent studies have used data from SDSS because of its unmatched statistical power. These data, while of very high quality compared to photographic plate measurements, are several magnitudes shallower than our MegaCam data and taken under less ideal conditions (with seeing a factor 2 larger). Conversely, **?** have used deep, high-quality HST imaging to measure galaxy alignments, finding no evidence for galaxy alignments within clusters. As in our analysis, **?** have considered spectroscopically-confirmed cluster members, thus in addition to the superior photometry, both works have a cleaner member sample, which is key to the interpretation of the signal. **?** also used a sample of spectroscopically-confirmed group members, plus a shape measurement method that was specifically calibrated to weak lensing measurements (**?**), and found no significant evidence for alignments. Finally, **?** measured galaxy alignments in photometrically-selected galaxy groups and clusters in SDSS Stripe 82, fully accounting for photometric redshift uncertainties, and constrain alignments to similar values as those found here.

The fact that all recent measurements that use high-quality imaging and properly calibrated shape measurements have yielded null detections (**????**, plus the present study) leads us to conclude that there is no evidence for intrinsic alignments of satellite galaxies in galaxy groups or clusters to the level of uncertainty achievable with current datasets (both statistical and systematic).

4.6.   Contamination to cosmic shear measurements

In this section we explore the impact that the measured galaxy alignments in clusters can have on future cosmic shear measurements. We quantify the contribution of intrinsic alignments to cosmic shear measurements through the matter and intrinsic alignment power spectra, which can be defined as

$$
\begin{aligned}
\left\langle \tilde{\gamma}^{I*}(\mathbf{k})\tilde{\gamma}^{I}(\mathbf{k}') \right\rangle &= (2\pi)^3 \delta_D^{(3)}\left(\mathbf{k}-\mathbf{k}'\right) P_{II}(\mathbf{k}) \\
\left\langle \delta^{*}(\mathbf{k})\tilde{\gamma}^{I}(\mathbf{k}') \right\rangle &= (2\pi)^3 \delta_D^{(3)}\left(\mathbf{k}-\mathbf{k}'\right) P_{GI}(\mathbf{k}).
\end{aligned}
\tag{4.11}
$$

Here, $\tilde{\gamma}^{I} = (1+\delta_g)\gamma^{I}$ is the (projected) ellipticity field weighted by the galaxy density, δ_g, and $P_{II}(\mathbf{k})$ and $P_{GI}(\mathbf{k})$ are the II and GI contributions to the power spectrum including a prescription for nonlinear evolution (i.e, nonlinear power spectra, see **??**), respectively; δ^{*} is the complex conjugate of the Fourier transform of the matter density contrast, $\delta(\mathbf{r}) = (\rho(\mathbf{r})-\bar{\rho})/\bar{\rho}$ is the matter overdensity with respect to the average density of the Universe, $\tilde{\gamma}^{I*}$ indicates the complex conjugate of $\tilde{\gamma}^{I}$, and δ_D is a Dirac delta function.

Additionally, we translate the 3-dimensional power spectra discussed above into (observable) angular power spectra, C_ℓ, using the **?** approximation (e.g., **?**). We use a source redshift distribution given by

$$p(z) \propto z^\alpha \exp\left[-(z/z_0)^\beta\right], \tag{4.12}$$

where we fix the parameters α, β, and z_0 so that the median redshift of the model distribution reproduces the median redshift of the Kilo-Degree Survey (KiDS, **?**), $z_{med} \simeq 0.7$ (Kuijken et al., in prep). We split the lens sample in redshift bins of half-width $\Delta z = 0.1$ to illustrate the results obtained from a tomographic cosmic shear analysis (e.g., **?**). We use a narrow redshift bin covering $0.6 < z < 0.8$ for the GG and II power spectra, since this range is close to the one that maximizes the lensing signal in a KiDS-like tomographic analysis. The GI power spectrum is better captured by cross-correlating this redshift bin with one at low redshift; we choose $0.2 < z < 0.4$ as a compromise between a high intrinsic alignment efficiency and a large enough volume observed.

4.6.1. Linear alignment model

The simplest models for galaxy alignments predict that elliptical galaxies are aligned with a strength that is proportional to the tidal field (**?**) while spiral galaxies, which are aligned by angular momentum acquired during gravitational collapse, are aligned with a strength that is proportional to the square of the tidal field (**?**). On sufficiently large scales, all galaxies are predicted to experience an alignment proportional to the large scale gravitational potential (**?**). Thus a linear alignment model is usually employed to characterize large scale galaxy alignments (e.g., **????**).[9] We normalize the intrinsic alignment power spectra as in previous studies (**???**), matching to the SuperCOSMOS measurements of **?**. This normalization is also consistent with more recent observations (**???**).

Solid lines in Figure 4.12 show the angular power spectra, C_ℓ, from the linear alignment model. This model includes no contribution from alignments within haloes (so-called 1-halo terms) and therefore the II and GI power spectra are subdominant to the matter power spectrum at all scales.

Figure 4.12 also shows the expected angular power spectrum measurements of a reference cosmic shear survey with properties similar to KiDS with a redshift distribution as described above, with a sky coverage of 1,500 sq. deg. and a background source density of $n_{gal} = 10\,\text{arcmin}^{-2}$. We assume a coverage $30 \leq \ell \leq 3000$, and compute the expected C_ℓ measurements and uncertainties following **?**, in logarithmic bins in ℓ. The bottom panel of Figure 4.12 shows that the II contribution remains safely subdominant to statistical uncertainties expected for KiDS, but the GI contribution cannot be ignored, contaminating the GG power spectrum at the $\sim 10\%$ level.

4.6.2. Halo model

The linear alignment model aims to describe alignments at large scales and the alignments between central galaxies, because these are expected to be aligned with the host halo by the large scale gravitational potential. On smaller, nonlinear scales, galaxy formation will tend to misalign baryonic and dark matter (e.g., **??**), so the large-scale results from N-body

---

[9]This model is typically referred to as "nonlinear alignment model." However, this is a misnomer, since intrinsic alignments are still modeled as depending linearly on the tidal field; instead the name arises from the use of the nonlinear power spectrum in Equation 4.11. We therefore refer to it as linear alignment model throughout.

simulations are probably not directly applicable to galaxy alignments within haloes. Galaxy formation can also have a major impact on the power spectra (**??**), and the way these two effects interplay is unclear. We therefore require a prescription to predict the power spectra accounting for 1-halo term galaxy alignments. To this end, we employ the halo model of radial alignments introduced by **?**.

The main assumption of the halo model is that galaxies form and reside in dark matter haloes whose masses directly influence the (observable) properties of the galaxies they host. Additionally, one can assume that satellite galaxies in a halo are radially aligned toward the centre with a strength that can in principle be a function of the galaxy position in the halo, the host halo mass, and redshift. This is known as a *satellite radial alignment model*. The total alignment can be separated into a prescription for galaxies in haloes (the 1-halo term), and one between haloes (the 2-halo term). We assume that galaxies populate haloes following the halo occupation distribution of **?** and the halo mass and bias functions of **?**. More details about the ingredients of this halo model can be found in **?**. Given a model for radial alignments, $\gamma^I(\mathbf{r}, M, z)$, we calculate the power spectra through Equation 4.11.

This model only incorporates the information about the radial alignments studied in Section 4.5.1, by definition. In principle, it would be possible to include further constraints on the alignments from measurements such as those explored in Sections 4.5.2 and 4.5.3. However, these would be second order corrections to the cluster-scale radial component. In particular, the satellite-satellite alignment constraints woud be relevant on scales smaller than what will be probed by current and upcoming experiments; we therefore choose not to include them in the present analysis.

4.6.3. Impact of alignments within haloes on the power spectra

The halo model requires a prescription for the strength of small-scale radial alignments. In its simplest form this strength is constant with radius and halo mass. The power spectra derived from this model are shown as dashed lines in Figure 4.12, for an alignment strength $\bar{\gamma} = 0.21$ ($\bar{\gamma}$ is the 3-dimensional alignment strength derived from a projected measurement, γ^I; see **?**). This is the fiducial value adopted by **?**. In this work, we extend this prescription by assuming a radial alignment that depends on halo mass but not on distance within the halo. Such a model is fully consistent with our results, since we find a null signal at all radii.

We construct a mass-dependent alignment model using the present results, plus the intrinsic alignment measurements in galaxy groups from the Galaxy and Mass Assembly (GAMA) survey (**?**). We assume a power law for $\gamma^I(M)$, such that the mean ellipticity of satellite galaxies has the 2σ upper limits obtained in this study. We use the results for the augmented spectroscopic plus red sequence member sample, and choose to use the KSB measurement because, although the GALFIT constraint is less tight (i.e., more conservative), the contribution of each mass scale is weighted by the mass function. Since the mass function is an exponential function of mass, the overall alignment signal is dominated by lower mass objects. Since we use the constraint found for GAMA groups as a pivot, a smaller alignment strength in clusters will mean a larger overall contribution of alignments to a cosmic shear survey. Specifically, we use $\epsilon_+ < 0.0019$ at $M \simeq 10^{15}\,M_\odot$ and $\epsilon_+ < 0.019$ at a typical mass $M \simeq 10^{13}\,M_\odot$, corresponding to the 2σ upper limit for GAMA groups with $N_{\mathrm{gal}} \geq 5$ (**?**). Our model is therefore $\gamma^I(M) = (M/M_0)^\alpha$, constant with redshift, with $M_0 = 1.19 \times 10^9 M_\odot$ and $\alpha = -0.5$.[10] We note that the assumption of a single power law at all masses has no justification other

---

[10]The conversion between ellipticity and shear is given by $\gamma = \epsilon_+ / 2\mathcal{R}$, where $\mathcal{R}$ is the shear responsivity, which we assume to be equal to 0.87.
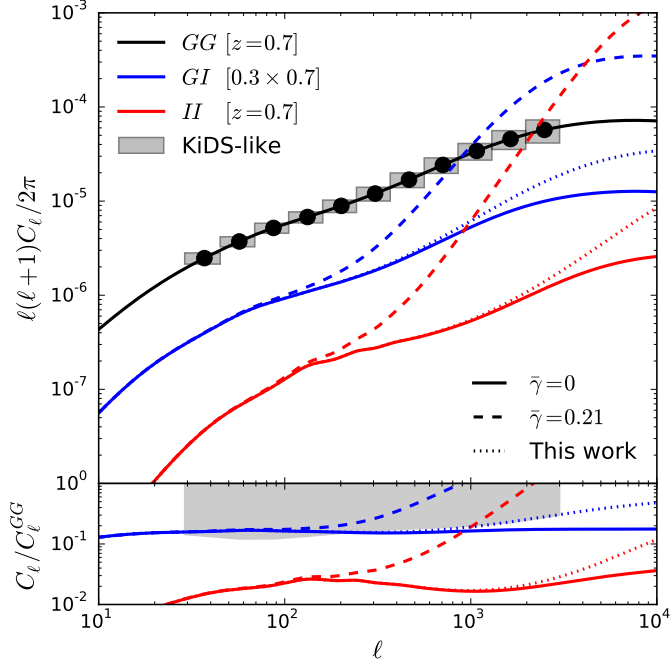
Figure 4.12: Effect of intrinsic alignments on the angular power spectra. *Top panel:* The black line shows the GG power spectrum, while blue and red lines show the GI and II power spectra, respectively. Solid lines show the linear alignment model with no small-scale intrinsic alignments, while dashed and dotted lines model the contribution of satellite galaxies with $\bar{\gamma} = 0.21$ as in **?** and with the mass-dependent 2σ upper limit on the alignment signal derived in this work (see Section 4.6.3), respectively. Grey boxes with black circles show the expected uncertainty levels on a KiDS-like survey covering 1,500 sq. deg. and with $n_{gal} = 10\,\mathrm{arcmin}^{-2}$. The *bottom panel* shows the ratio between the GI and II power spectra and the GG power spectrum, for each model. The shaded region shows values above the 1σ uncertainties in the anglar power spectrum for a KiDS-like survey, where GI and II contributions would dominate over statistical uncertainties.

than its simplicity. A more detailed halo model for intrinsic alignments will be presented in a forthcoming study (Cacciato et al., in prep), where we explore the impact of halo model assumptions on the predictions of the II and GI power spectra.

Dotted lines in Figure 4.12 show the intrinsic alignment power spectra predicted by the halo model for our adopted $\gamma^I(M)$. Since we constructed the model using 2σ upper limits on the measured alignments, the regions between the solid and dotted lines should be regarded as conservative estimates of the current uncertainties on the GI and II power spectra due to 1-halo term intrinsic alignments. As can be seen, both the GI and II power spectra remain subdominant to the GG power spectrum, which is not the case with the fiducial $\bar{\gamma} = 0.21$ model used by **?**. The GI angular power spectrum including our 1-halo term is ~70% higher than that predicted by the linear alignment model at $\ell \sim 3000$, which translates into an excess on the total (GG+GI+II) angular power spectrum of $\approx 10\%$, comparable to the statistical uncertainties expected at these scales. Note that at larger scales the GI power spectrum is dominated by linear alignments and the satellite contribution is well below the statistical uncertainties of KiDS. Therefore, we do not expect that cosmic shear analyses with KiDS will need to include a contribution by satellite galaxies in the modeling of intrinsic alignments, and we conclude that the linear alignment model should be a sufficient treatment of intrinsic

alignments for KiDS. We note that for a bin at $0.2 < z < 0.4$, the II power spectrum can be > 10% of the lensing (GG) power spectrum at the same redshift, but the uncertainties of a KiDS-like survey are much larger than at $z \sim 0.8$ because of the smaller volume probed. In any case, the linear alignment model captures any II contribution to sufficient accuracy. Therefore a treatment of intrinsic alignments in KiDS cosmic shear analyses can rely on the linear alignment model, similar to the cosmic shear analysis of CFHTLenS data by **?**. We expect the situation to be similar for the Dark Energy Survey (DES)[11], which will have three times as much area as KiDS but otherwise similar characteristics. This may not be the case for larger surveys, for which the contribution of satellite galaxies to intrinsic alignments must be characterized to higher precision.

4.7.   Conclusions

We have compiled a large sample of galaxies with spectroscopic redshifts in the direction of 90 galaxy clusters in the redshift range $0.05 < z < 0.55$, selected as part of MENeaCS and CCCP. We select cluster members using the shifting gapper technique, which uses phase space information, for a total 14,576 cluster members. We use these members to estimate dynamical masses using the simulation-based scaling relation between velocity dispersion and cluster mass of **?**. The sample has a median redshift $z = 0.14$ and a median mass $M_{200} \sim 7 \times 10^{14}\,M_\odot$, in good agreement with the weak lensing masses estimated by **?**.

We quantify the alignment of galaxies within clusters using 14,250 cluster members for which we are able to measure their shapes either with KSB or GALFIT, after showing that the ellipticities measured by both methods are consistent (Figure 4.6). Both methods take different approaches to measuring galaxy shapes and therefore provide an important consistency check. We confirm that our analysis is free of significant systematic effects by measuring the average alignment of both foreground galaxies and stars. The signal from foreground galaxies is consistent with zero; the signal from stars is significantly different from zero, but at a level of $\langle \epsilon_+ \rangle \sim 10^{-4}$, an order of magnitude lower than measurement uncertainties (Figure 4.7).

We measure three different alignments: the radial alignment of satellite galaxies toward the BCG, the alignment of satellites with the BCG orientation, and the radial alignment of satellites toward each other. Each probes a different, but not necessarily independent, effect. We find no evidence for any of these alignments (Figures 4.8 to 4.11). In particular, we constrain the average ellipticity of satellites toward BCGs to $\langle \epsilon_+ \rangle = -0.0037 \pm 0.0027$ with KSB and $\langle \epsilon_+ \rangle = 0.0004 \pm 0.0031$ with GALFIT, at 68% confidence, within r_{200}. Similarly, there is no evidence of galaxy alignments when splitting the sample by cluster (redshift, mass, or dynamical state) or galaxy (color or luminosity) properties. Selecting additional cluster members through the red sequence allows us to extend the sample to ~20,000 galaxies with an estimated contamination of < 10% from red sequence interlopers (Figure 4.4). All signals from this enlarged sample are also consistent with zero.

We include this constraint on the radial alignment of galaxies within high-mass haloes, together with a measurement at the group scale (**?**), in a halo model framework, and derive the current uncertainty on the angular power spectrum given by intrinsic alignments within haloes (a 1-halo term). We find that the total (GG+GI+II) angular power spectrum predicted from our alignment model (see Section 4.6.3) is, at most, 10% higher than the total power spectrum predicted by the linear alignment model at the smallest scales probed by

---

[11]http://www.darkenergysurvey.org

KiDS, $\ell \sim 3000$. This level of contribution from satellite galaxies will not be relevant for cosmic shear measurements with KiDS or DES (see Figure 4.12). We conclude that the linear alignment model is a sufficient description of intrinsic alignments for KiDS, but the situation may be different for significantly larger surveys.